# Fragmentation of drops falling through a miscible liquid with and without drop-drop interactions

Nakajima, Rina

Hayashi, Kosuke

(Citation)
International Journal of Multiphase Flow,153:104134

(Issue Date)
2022-08

(Resource Type)
journal article

(Version)
Accepted Manuscript

# Fragmentation of drops falling through a miscible liquid with and without drop-drop interactions

Rina Nakajima[a], Kosuke Hayashi[b,*]

[a] *Tennoji High School Attached to Osaka Kyoiku University, 4-88 Minamihorikawa-machi Tennoji Osaka, 543-0054 Japan*

[b] *Graduate School of Engineering, Kobe University, 1-1 Rokkodai Nada Kobe Hyogo, 657-8501 Japan*

**Abstract**

Experiments on liquid drops falling through a miscible liquid are carried out. Drops deform into vortex rings and then fragment into smaller drops due to the Rayleigh-Taylor instability. The number, $m$, of smaller drops is measured for large Archimedes numbers, $Ar$. The influence of the interaction between two vortex rings on the fragmentation is also discussed. The $m$ of single drops exhibits a random nature; the probability distribution can be approximated with the normal distribution. An empirical correlation of the mean, $\overline{m}$, of $m$ is developed to cover a wide range of $Ar$. Numerical predictions of $m$ of single drops reveal that the growth rate of a vortex ring is the key factor in determining $\overline{m}$. Experiments on two drops falling inline show that the interactions between vortex rings can be classified into three types, and, in all interaction types, the presence of the leading ring decreases $\overline{m}$ of the trailing ring.

*Keywords:* vortex ring, drop breakup, Rayleigh-Taylor instability, miscible fluid

*Corresponding author

*Email address:* hayashi@mech.kobe-u.ac.jp (Kosuke Hayashi)

## 1. Introduction

When a liquid drop sinks down in a stagnant pool of miscible liquid, the drop shape changes from spherical to mushroom-like to disk-like to torus (ring) and then a cascade of fragmentation takes place due to the onset of hydrodynamic instabilities. The fragmentation of a drop is of great interest not only due to its beauty of flow pattern, but also due to its fundamental importance in a mixing process of two miscible liquids. Tomlinson (1864a,b) observed the behavior of a drop falling through a liquid with various pairs of liquids and described it accompanying detailed sketches. Thomson and Newall (1886) carried out experiments on a single drop falling into a stagnant liquid to investigate the fragmentation phenomena from a hydrodynamic point of view. They pointed out that the density difference is necessary for the formation of a vortex ring and the liquid viscosity plays a crucial role, i.e. the vortex motion diffuses from the boundary into a drop by the action of viscosity, which causes breakup of the disk-like shape into torus. They also pointed out that child drops generated from their parent vortex ring by fragmentation are connected by thin liquid threads, so that the action of an effective interfacial tension (Korteweg, 1901; Kostin et al., 2003) was negligible in the motion of the miscible liquids in their experiments.

After a century from the work of Thomson and Newall (1886), Arecchi et al. (1989, 1991, 1996) carried out a series of experimental studies on the motion of a vortex ring and its fragmentation to find a scaling law governing the phenomena (Residori et al., 2007). Arecchi et al. (1989) described the fragmentation process as follows: the Kelvin-Helmholtz instability induces a deformation of a drop from spherical to mushroom-shape. The falling motion of the drop is retarded and the drop becomes thinner and wider, so that a vortex ring is formed. Disturbances then grow due to the Rayleigh-Taylor instability and a break of axisymmetry of the vortex ring takes place followed by fragmentation. They derived the fragmentation number, $F$ $(= \Delta\rho g V/\mu_0 D)$, which is the ratio of the time scale of mass diffusion to that of the falling motion of a drop, and concluded that $F > F_c$ is the condition for the onset of fragmentation, where $\Delta\rho$ is the density difference, $g$ is the magnitude of the acceleration of gravity, $V$ is the drop volume, $\mu_0$ is the viscosity of the bulk liquid, $D$ is

the diffusion coefficient, and $F_c$ is the critical fragmentation number. Arecchi et al. (1991) introduced the Schmidt number, $Sc$ ($= \mu_0/\rho_0 D$), in addition to $F$ to correlate the number, $m$, of child drops in terms of $F$ and $Sc$, where $\rho_0$ is the density of the bulk liquid, that is, a graphical correlation showed that data points of each $m$ collapse on the lines given by $F/Sc^{\alpha(m)} = \beta(m)$. Here $\alpha$ and $\beta$ are functions of $m$. This expression works fairly well for $m \geq 5$.

Shimokawa et al. (2016) experimentally studied the fragmentation of single drops falling through a stagnant liquid and confirmed that the increase in $F$ increases $m$ as reported by Arecchi et al. (1991). Numerical simulations of the motion of a vortex ring were also conducted. The results showed that the circulation of a vortex ring suppresses the Rayleigh-Taylor instability, which implies that stronger the circulation, more stable the vortex ring is. Shimokawa and Sakaguchi (2017, 2019) conducted the experiment with several drop sizes, density differences and viscosities. They pointed out that the dependence of $m$ on $Sc$ is not clear in their experimental range, whereas $m$ can be well correlated in terms of the Archimedes number, $Ar$. The $m$ increases with increasing $Ar$, in other words, the increase in the gravitational force enhances the Rayleigh-Taylor instability, while the increase in the viscous force mitigates it. As pointed out by Shimokawa et al. (2016), the dimensionless groups have the relation, $Ar = \gamma F/Sc$, by definition, where $\gamma = 3/(4\pi)$. Hence the scaling of $m$ in terms of $Ar$ is comparable with the relation, $F/Sc^{\alpha} = \beta$, whereas in the former the diffusion coefficient plays no role in $m$ because of $\alpha = 1$. Although the $m$ data collapsed onto a single curve by using $Ar$, the range of $Ar$ in their experiments is $Ar \leq 80$ and our knowledge on the dependence of $m$ on $Ar$ for a larger $Ar$ range is still lacking.

The above-mentioned studies in the literature dealt with fragmentation of single drops. Although interactions between vortex rings have been of great interest and various studies on vortex rings moving along a common axis of symmetry have been done so far (Thomson, 1883; Oshima et al., 1975; Kojima et al., 1984; Meleshko, 2010; Meleshko et al., 2012), to our best knowledge, fragmentation of multiple liquid drops in a miscible liquid under their interactions has not been studied in detail yet.

In this study, the number of child drops formed in the first fragmentation of a single

vortex ring was measured for $Ar$ = 290, 480 and 930, which are larger than $Ar$ tested in Shimokawa and Sakaguchi (2017, 2019), for further understanding of the effects of $Ar$ on $m$. Then the influence of the interaction between two vortex rings on the fragmentation was investigated in the large $Ar$ condition. We focused only on the first fragmentation, and the subsequent fragmentation in the breakup cascade is outside the scope of the present study.

## 2. Experimental

Figure 1 shows the experimental setup. The width, depth and height of the water tank were 0.150, 0.150 and 0.200 m, respectively. The upper water tank was used to slowly fill up the main tank with water. The tanks were made of transparent acrylic resin. Drops were generated from the needle (Terumo, NN-2138R) attached to the syringe (Terumo, SS-50ESZ). The height of the needle tip (the initial height of a drop) is of importance in the formation of vortex ring. Thomson and Newall (1886) carried out experiments with various combinations of liquids and examined three different initial heights, i.e. 0, 1/2 and 3/4 inches. They classified the state of drops after impacting on the free surface into either 'ring', 'splash', 'uncertain', 'blob' or 'doubtful', and for some combinations of liquids the drop state depended on the initial height. In the experiments of Arecchi et al. (1989), a drop kept at the needle tip touched to the free surface and was sinked into the liquid pool by the action of surface tension; this condition corresponds to the zero initial height in Thomson and Newall (1886). On the other hand, in the series of experiments by Shimokawa et al. (Shimokawa et al., 2016; Shimokawa and Sakaguchi, 2017, 2019), drops fell from the needle tip placed 8 mm above the free surface. The initial height was also set to 8 mm in the present experiment and good rings could be obtained in the present experimental range. By using the syringe pump (YMC, YSP-201), the syringe was pushed at a constant rate, with which the time interval, $\Delta t$, between two drops in the two-drop experiment was 3.00 s with the sample standard deviation of 0.07 s.

We observed the motion of drops in water by using two video cameras (Sony, FDR-AX60). They were mounted on supporting frames so as to take images of side and top views of drops and were synchronized in each recording. The liquid for drops was colored by

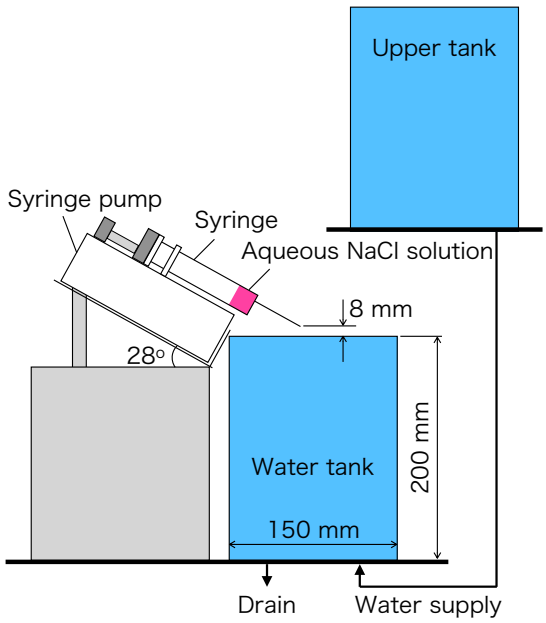


Figure 1: Experimental setup.

adding a red-food color (Kyoritsu Foods) for visualization. The number of child drops in the first fragmentation was counted from the video images as follows. The formation of a vortex ring was observed from both top and side video images. The vortex ring became thinner as it laterally grew. During the growth of the ring, smaller drops (child drops) were formed from some part of the ring, and the remaining part of the ring got thinner and thinner and the resultant filament did not fragment. The child drops went to the second fragmentation, and therefore, the child drops could be distinguished from the filament. We rejected samples when the drop images were not clear enough to count the number of child drops.

Tap water and an aqueous-NaCl (Sodium Chloride, 99.5% purity) solution were used for the bulk liquid and drops, respectively. In the single-drop experiment, we used three weight concentrations, $C$, of NaCl, i.e. 0.6, 2.2 and 3.0%. The experiments were carried out at atmospheric pressure and the liquid temperatures were 25°C for the former two and 16°C for the latter. The densities, $\rho$, were 1001, 1012 and 1019 kg/m$^3$ for 0.6, 2.2 and 3.0% (Rogers and Pitzer, 1982), respectively, and the viscosities, $\mu$, were 0.91, 0.93 and 1.1 mPa·s (Ozbek et al., 1977). The addition of the coloring agent was confirmed to increase the density

by 0.78 kg/m$^3$ and the viscosity by 2%. The density and viscosity, $\rho_0$ and $\mu_0$, of water were 997 kg/m$^3$ and 0.89 mPa·s, respectively, at 25°C and 999 kg/m$^3$ and 1.1 mPa·s at 16°C, so that the density differences, $\Delta\rho$, between the aqueous-NaCl solutions and water were 5.0, 15.7 and 21.2 kg/m$^3$ at $C = 0.6$ and 2.2 and 3.0%, respectively. Although the relative viscosity difference is larger than the relative density difference, the effects of the former on the growth of perturbations due to the Rayleigh-Taylor instability are small as discussed in Appendix C. Shimokawa and Sakaguchi (2019) used an aqueous glycerol solution and an aqueous ferric sulfide solution for the bulk fluid and drops, respectively. They added polyethylene glycol (PEG) into both fluids to make the viscosities close. This method, however, may bring another uncertainty in the analysis of the fluid motion since PEG has non-Newtonian characteristics. We, therefore, did not use the viscosity tuning technique in the present experiment. The diffusion coefficient, $D$, of the aqueous-NaCl solution in water was estimated as $1.6 \times 10^{-9}$ m$^2$/s (Riquelme et al., 2007). The Schmidt number was therefore 560. In the two-drop experiment, we used the aqueous-NaCl solution of $C = 0.6\%$.

The radii, $r$, of drops were measured from images of drops just before the detachment from the needle tip. Positions, $h_F$, of the first fragmentation measured from the free surface were evaluated from side images.

Additional experiments with lower NaCl concentrations were also carried out to confirm the characteristics of the number of child drops for $Ar < 100$. See Appendix A for the details.

## 3. Results and Discussion

### *3.1. Fragmentation of single drop*

#### *3.1.1. Relative frequency density of number of child drops*

The mean $r$ were 1.68 mm and 1.69 mm at $C = 0.6$ and 2.2%, respectively, and was 1.42 mm at $C = 3.0\%$, and the uncertainties in the mean radii at 95% confidence were less than 0.03 mm. The water tank was therefore much larger than the drop size, so that the effects of the tank wall on the drop motion were negligible. In the present experiment,

$F = 6.8 \times 10^5$, $2.2 \times 10^6$ and $1.4 \times 10^6$ for $C = 0.6$, 2.2 and 3.0%, respectively, which meet the fragmentation criterion proposed by Arecchi et al. (1989), i.e. $F > F_c$ ($= (2.8 \pm 0.1) \times 10^5$). The Archimedes number defined by

$$Ar = \frac{\rho_0 \Delta\rho g r^3}{\mu_0^2} \quad \left( = \frac{3F}{4\pi Sc} \right) \tag{1}$$

were 290, 480 and 930 for $C = 0.6$, 3.0 and 2.2%, respectively.

Figure 2 shows an example of the falling motions of single drops observed from the horizontal direction. The drop takes a mushroom-like shape in the first image (i), whereas it changes into torus (ii) followed by formation of child drops by fragmentation (iii). The child drops then proceed to the second fragmentation (iv). The thin threads connecting the child drops do not break up into smaller drops, which confirms as pointed out by Thomson and Newall (1886) that the action of the interfacial tension is negligible in the present miscible system. The first fragmentation took place at $h_F = 19.6$ mm in average for 194 samples. In most of the experimental runs, $h_F$ were less than 30 mm, i.e., the relative frequency densities of $h_F$ were 18%, 49% and 18% for the bins of $[0, 10$ mm), $[10, 20$ mm) and $[20, 30$ mm), respectively.

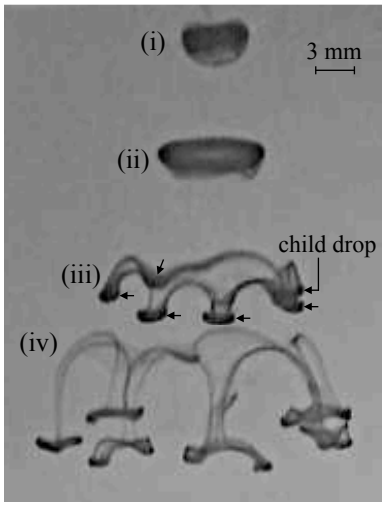


Figure 2: Example of drop motion (side view). (i) mushroom-like shape; (ii) ring; (iii) formation of child drops ($m = 6$); (iv) onset of second fragmentation from child drops. The times elapsed from drop impact are 0.5(i), 1.7(ii), 4.3(iii) and 7.7 s(iv).

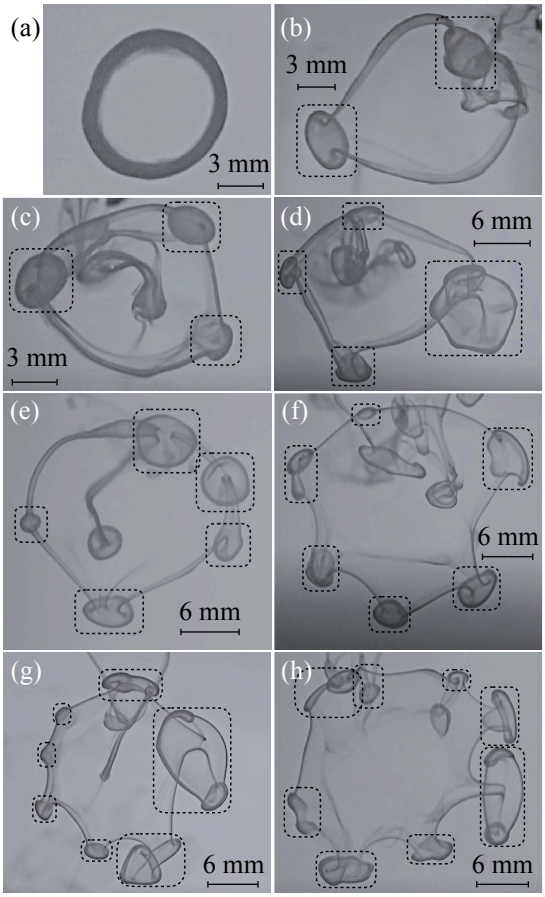


Figure 3: Examples of fragmentation (top view; $C = 0.6\%$). (a) vortex ring before fragmentation; rings in (b)-(h) are $m = 2,\ 3,\ 4,\ 5,\ 6,\ 7,\ 8$. The dotted lines indicate child drops. The times elapsed from drop impact on the free surface to the moments of the photos are 2.2 s, 4.8 s, 3.3 s, 5.4 s, 6.4 s, 8.9 s, 6.0 s and 8.4 s from (a) to (h).

Figure 3(a) is a vortex ring before the onset of fragmentation. Vortex rings were falling down through water and child drops were formed from some parts of the rings. Fig. 3(b) is an example of $m = 2$, in which the dotted lines indicate child drops. A ring with three child drops ($m = 3$) is shown in Fig. 3(c). In Fig. 3(d) for $m = 4$, one of the four child drops (on the right side of the image) grew slightly faster than the others. The formations of child drops were not always simultaneous. Child drops formed from a ring earlier than the others could be in the second fragmentation while the other drops were still in the first fragmentation stage. Rings of larger $m$ are shown in (e)-(h).

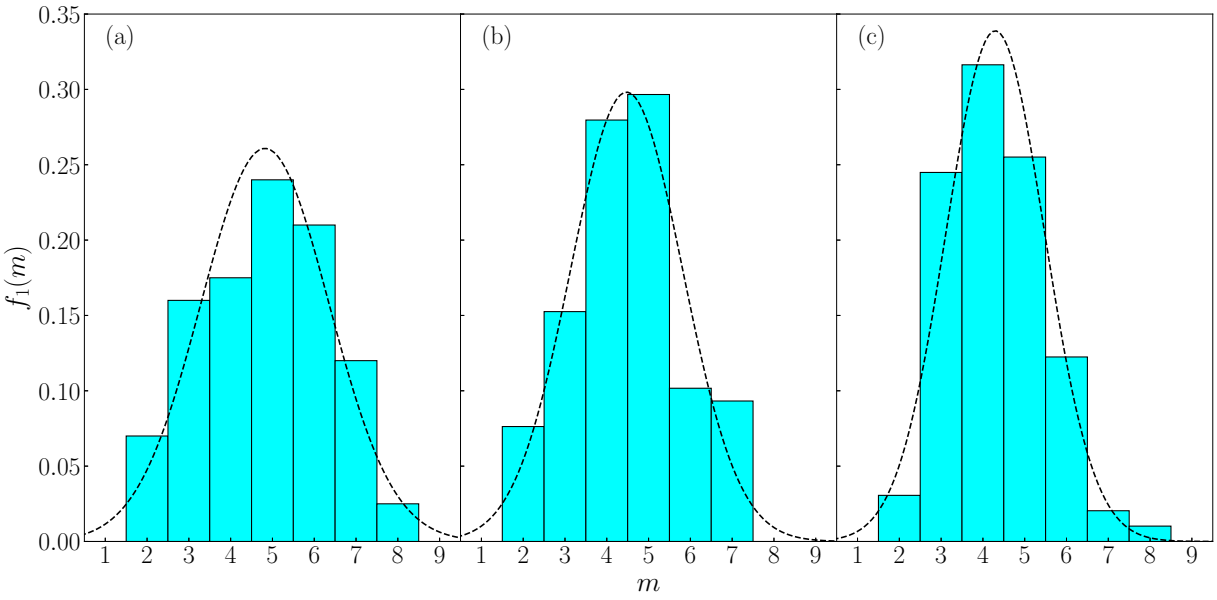


Figure 4: Relative frequency density, $f_1(m)$, of fragmentation of single drops. (a) $Ar = 290$, $C = 0.6\%$, 200 samples, $\overline{m} = 4.82$, $\sigma = 1.5$; (b) $Ar = 480$, $C = 3.0\%$, 118 samples, $\overline{m} = 4.47$, $\sigma = 1.3$; (c) $Ar = 930$, $C = 2.2\%$, 98 samples, $\overline{m} = 4.3$, $\sigma = 1.2$. The dashed line is the normal distribution for the mean and sample standard deviation of $m$.

Figure 4(a) shows relative frequency densities, $f_1(m)$, of $m$ at $Ar = 290$, where the relative frequency density is defined as the frequency of fragmentation event with $m$ child drops divided by the total number of samples and the width of the bin ($\Delta_m = 1$) and the subscript 1 denotes the single drop case. The $m$ does not take a unique value, but ranges from two to eight. The fragmentation of $m = 1$ does not appear in the data. Kambe and Takao (1971) analyzed the deformation of a circular vortex ring. The vortex ring is not distorted with disturbances of the 0th mode ($m = 0$), which induces a slight change in the ring radius. The 1st mode ($m = 1$) may cause a little change in the path of the translational motion, but the disturbances of this mode does not contribute to the shape deformation. The circular ring is deformed into a twisted shape (Arecchi et al., 1989) by disturbances of $m \geq 2$. This explains the reason of $f_1(1) = 0$.

A similar random nature of the fragmentation was reported in Shimokawa et al. (2016) though the standard deviations in their experiment were smaller than the present one. The

larger standard deviation in the present data can be attributed to the lower liquid viscosity as follows. The viscous effect suppresses the appearance of large $m$ since the viscous dissipation dampens disturbances; especially the kinetic energies of large wave number disturbances are to be quickly dissipated. Hence, it is expected that larger the viscosity is, narrower the $f_1(m)$ distribution is. An example for this viscosity dependence can be found in Shimokawa and Sakaguchi (2019), which also reported that the increase in the drop radius increases both the mean $m$ and the standard deviation. Applying Pearson's $\chi^2$ test with 5% significance level does not reject a similarity between the distribution of $f_1(m)$ and the normal distribution, which is drawn in the figure by the dashed line, though $m$ is a discrete variable. The mean value, $\overline{m}$ ($= \sum m f_1(m) \Delta_m$), of $m$ is 4.82 and the sample standard deviation, $\sigma$, is 1.5. The $f_1(m)$ for $Ar = 480$ and 930 are shown in Figs. 4(b) and (c), respectively. The $\overline{m}$ slightly decreases with increasing $Ar$, i.e. $\overline{m} = 4.47$ and 4.3 at $Ar = 480$ and 930, respectively. The data imply that the increase in $\Delta\rho$ tends to slightly decrease $\sigma$. The shapes of $f_1(m)$ at $Ar = 480$ and 930 can also be approximated by the normal distribution.

*3.1.2. Correlating fragmentation mode in terms of Ar*

Figure 5 shows $\overline{m}$ plotted against $Ar$. The data for $Ar \leq 80$ were quoted from Shimokawa and Sakaguc (2017, 2019) and the details of the present data at $Ar = 13$, 47 and 97 are given in Appendix A. Shimokawa and Sakaguchi (2017) pointed out that their data imply the relation, $\overline{m} \propto Ar^{1/3}$. However, the following fitting equation (the dashed line in the figure) based on the relation gives $\overline{m}$ much larger than the present data for $Ar > 100$ (the star symbols):

$$\overline{m} = 1.31 Ar^{1/3} \tag{2}$$

On the other hand, as shown by the solid line, $\overline{m}$ can be simply fitted as

$$\overline{m} = \frac{4.7}{1 + (0.197Ar)^{-1}} \tag{3}$$

whose functional form is based on the assumptions that (1) $\overline{m} \to 0$ as $Ar \to 0$ since a drop does not breakup in a system of $\Delta\rho = 0$ (Thomson and Newall, 1886) and in an

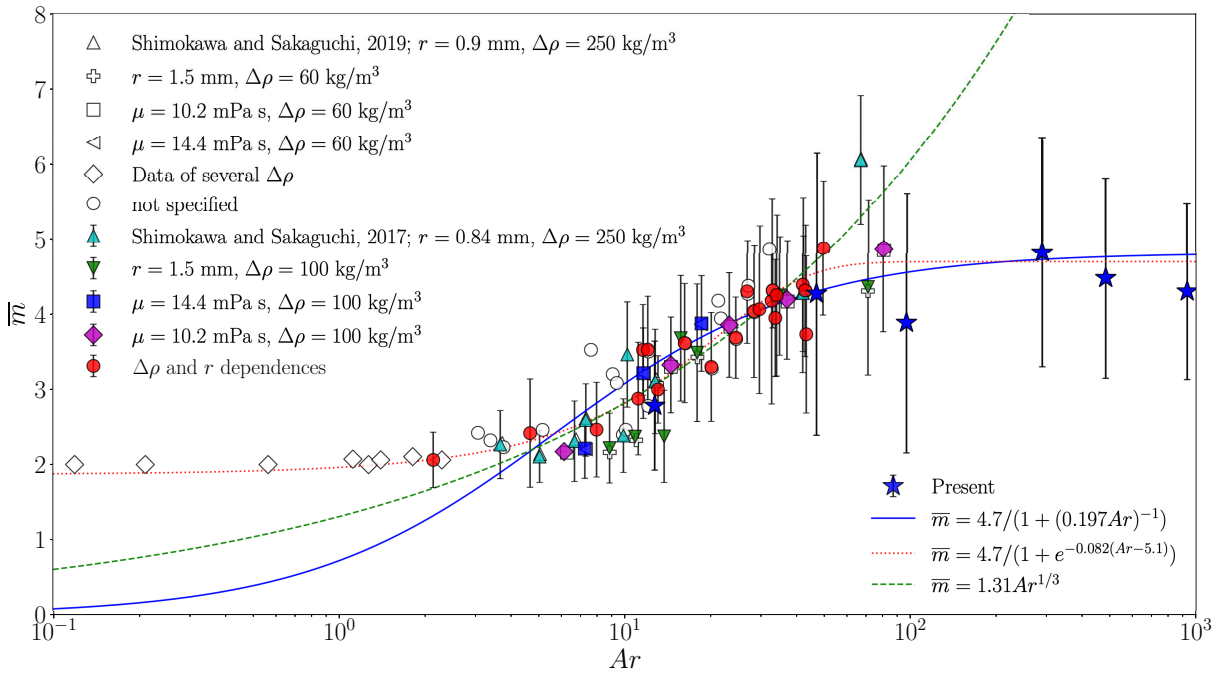


Figure 5: Number, $\overline{m}$, of fragmentations plotted against Archimedes number, $Ar$. The open symbols were quoted from Shimokawa and Sakaguchi (2019) and the closed symbols except for the star (present), were quoted from Shimokawa and Sakaguchi (2017).

extremely viscous system, in which disturbances are immediately dampened out by viscous dissipation, and (2) $\overline{m}$ does not depend on $Ar$ at large $Ar$. The fitting equation expresses well the data, except for $Ar < 4$, in which $\overline{m}$ is almost constant ($\approx 2$) in the data of Shimokawa and Sakaguchi (2019). At small $Ar$, the inertial and gravitational forces are much smaller than the viscous force and there is a possibility that the competition between the viscosity and the mass diffusion, i.e. the Schmidt number, plays a role in the onset of fragmentation. A better agreement with the data including the small $Ar$ range can be obtained by using the sigmoid function (the dotted line), that is,

$$\overline{m} = \frac{4.7}{1 + e^{-0.082(Ar-5.1)}} \tag{4}$$

This equation agrees with the available data although it gives $\overline{m} = 1.9$ even in the limiting case, $Ar \to 0$, which is inconsistent with the fact that no fragmentation takes place when $\Delta\rho = 0$. In addition, the slight reduction of $\overline{m}$ in the large $Ar$ range is not reproduced.

Shimokawa and Sakaguchi (2019) developed a numerical method for predicting $m$. Its brief description is given in the following. The change in the radius, $R(t)$, of a vortex ring is given by (Turner, 1957)

$$R(t) = \sqrt{R(0)^2 + \alpha t} \tag{5}$$

where $R(0)$ is the initial radius, and $t$ is the time. The $\alpha$ is the rate of change in the difference of the area, $\pi R^2(t) - \pi R^2(0)$, and is given by

$$\alpha = \frac{\Delta\rho g V}{\pi \rho_0 \Gamma} \tag{6}$$

where $V$ is the volume of a vortex ring, and $\Gamma$ is the circulation. By assuming that disturbances of the wave length, $\lambda$ $(= 2\pi R(t)/m)$, for the mode $m$ are formed on the ring, the wave number is given by

$$k(t) = \frac{m}{R(t)} \tag{7}$$

The rate, $n(k)$, of growth of the disturbance is evaluated by solving the characteristic equation for the Rayleigh-Taylor instability of a liquid superposed on a lighter liquid (see Appendix B). The rate of change of the magnitude, $A_m(t)$, of the disturbance is expressed as $A_m^{-1} dA_m/dt = n(k)$. Integrating this equation with the initial condition of $A_m(0)$ yields

$$A_m(t) = A_m(0) e^{\int_0^t n(k)dt} \tag{8}$$

The evolutions of $A_m(t)$ are calculated for each $m$ by numerically integrating the above equation, and the mode, whose $A_m$ becomes unity first, is selected as the mode actually appearing in the fragmentation. The initial value, $A_m(0)$, is randomly selected using the normal distribution with the standard deviation of $10^{-3.5} e^{-0.015m^2}$, which was obtained by Shimokawa and Sakaguchi (2019) so as to reproduce the $\overline{m}$ data of their experiments. A relative frequency density, $f_1(m)$, is obtained by simulating the growth of disturbances for various $A_m(0)$, and then, $\overline{m}$ is evaluated with $f_1(m)$.

The $\alpha$ in Eq. (5) can be evaluated using the following empirical correlation (Shimokawa and Sakaguchi 2019):

$$\frac{\alpha}{\nu} = c_1 Ar + c_2 \tag{9}$$

where $c_1 = (4.30 \pm 0.44) \times 10^{-2}$, $c_2 = (-15.99 \pm 6.04) \times 10^{-2}$, and $\nu$ is the kinematic viscosity. Although this correlation was developed for the data of $Ar < 25$, Shimokawa and Sakaguchi (2019) obtained reasonable predictions for their experimental range of $Ar \leq 80$.

Figure 6 shows $\overline{m}$ predicted using the numerical method (the cross symbols). Table 1 shows the conditions of the simulations: the fluid properties and the drop radius were randomly selected in the ranges for examining various combinations of the parameters, the initial ring radius was set to $R(0) = 2r/3$. The total number of the simulations were 400 and 50 samples were taken for each simulation to evaluate $\overline{m}$. The increase in $Ar$ almost monotonically increases $\overline{m}$ for $Ar < 40$ and the predictions agree with the data and the correlation, Eq. (4). A bifurcation of the $\overline{m}$ curve however takes place at $Ar \sim 40$. One of the curves continuously increases with increasing $Ar$, while the other takes values in-between three and four up to about $Ar = 100$ and then increases again. The behavior of $\overline{m}$ is sensitive to the numerical condition in this range. The predictions with large scatter possibly describe the large variances in the experimental data in the large $Ar$ range. The predictions largely deviate from the present data at $Ar = 480$ and 930. We obtained $\overline{m} \sim 2$ in some cases even at large $Ar$. In those cases, $n(k)$ for $m = 2$ was initially the largest among the modes tested and that mode quickly reached the criterion, $A_2(t) = 1$. The solid line represents the $m$-$Ar$ curve obtained by the model in Shimokawa and Sakaguchi (2019). It agrees well with the present prediction for the upper curve up to $Ar = 100$ although the latter shows the bifurcation for $Ar > 40$ and some scatter even for $Ar < 40$. It should be noted that Shimokawa and Sakaguchi (2019) do not describe the number of datapoints and how they set the fluid properties, the drop radius and the initial ring radius for drawing the $m$-$Ar$ curve. The scatter in the experimental data of Shimokawa and Sakaguchi (2017, 2019) and in the present prediction implies a possibility that another dimensionless parameter affects $\overline{m}$ although $Ar$ would be the primal one.

Let us discuss the physical meaning of Eq. (9) from a mechanical point of view. Equation (9) can be approximated as $\alpha/\nu \sim c_1 Ar$. By substituting Eq. (1) and $\alpha = 2R\dot{R}$ into this equation, we obtain

$$2\mu_0 R\dot{R} \sim c_1 \Delta\rho g r^3 \tag{10}$$

Table 1: Numerical conditions. The parameters were randomly determined within the ranges represented by the upper and lower bounds. The initial ring radius $R(0)$ was given as $R(0) = 2r/3$ in all the simulations.

| | lower bound | upper bound |
|---|---|---|
| $Ar$ | 5 | 1000 |
| $\rho_0$ [kg/m$^3$] | 997 | 1120 |
| $\Delta\rho$ [kg/m$^3$] | 4 | 100 |
| $r$ [mm] | 1.0 | 2.5 |
| mean of $A_m(0)$ | $10^{-4}$ | $10^{-3}$ |

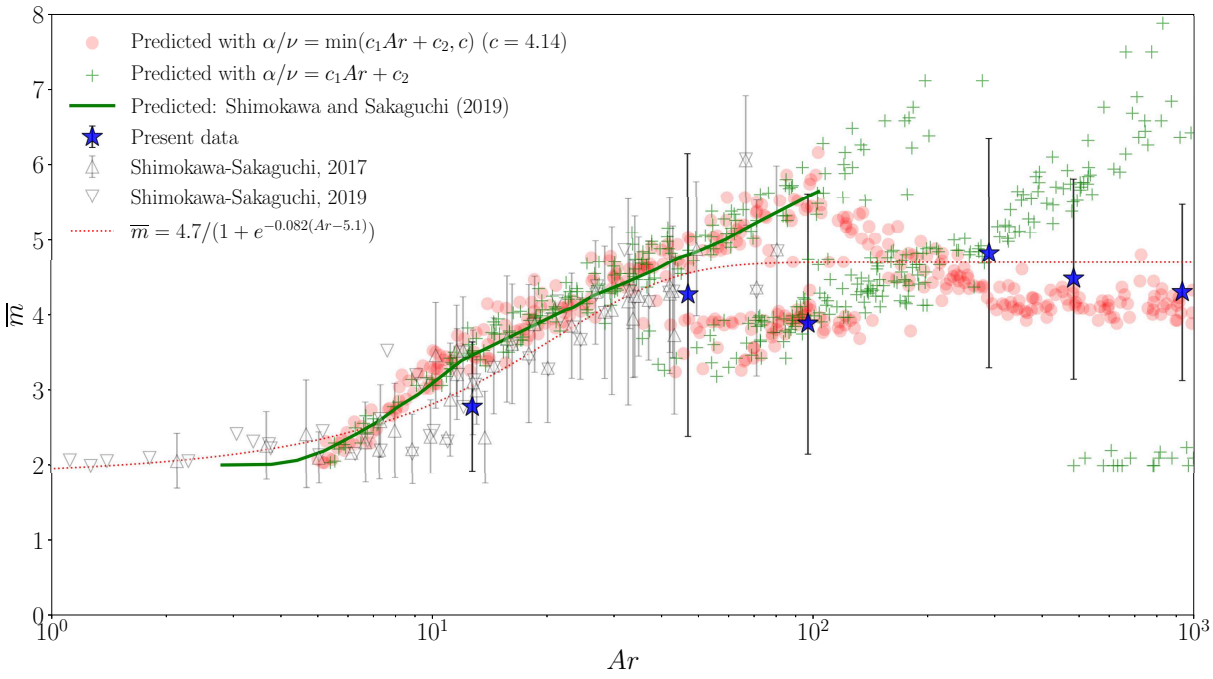


Figure 6: Number, $\overline{m}$, of fragmentations predicted using the method proposed by Shimokawa and Sakaguchi (2019) (the cross symbols). The closed circles are predictions obtained using Eq. (18) for $\alpha$. The solid line represents the predictions given in Shimokawa and Sakaguchi (2019) which agree with the cross symbols.

where $\dot{R} = dR/dt$. A ring of the height, $h$, expands laterally at the rate of $\dot{R}$. The order of magnitude of the velocity gradient can be evaluated as $\dot{R}/h$, and therefore, that of the viscous stress is $\mu_0\dot{R}/h$. The area, on which the viscous stress acts along the circumference of the ring, is evaluated as $2\pi Rh$. Hence, the order of magnitude of the viscous force is

expressed as

$$F_\mu \sim \mu_0 \frac{\dot{R}}{h} \cdot 2\pi R h, \tag{11}$$

With this expression for $F_\mu$, Eq. (10) can be rewritten as

$$F_\mu \sim c_1' F_g \tag{12}$$

where $F_g$ is the net gravitational force, $F_g = \Delta\rho g V$, $h = [2V/(\pi^2 R)]^2$, and $c_1' = 3c_1/4$. This relation represents that a part of the work done by the gravitational force acting on a ring is used for the lateral growth of the ring and is dissipated by the viscosity. Substituting the value of $c_1$ into the expression gives the estimation, $F_\mu/F_g \sim 0.032$. Thomson and Newall (1886) reported that if the viscosity is too large, the vortex motion is quickly dampened by the viscous dissipation so that the drop shape cannot develop to a ring. The $F_\mu$ much smaller than $F_g$ is consistent with the fact that the correlation of $\alpha/\nu$ was developed for clear rings (Shimokawa and Sakaguchi, 2019).

Since the predictions with Eq. (9) do not agree with the data for the large $Ar$ range, a modified correlation of $\alpha$ is examined in the following. The Archimedes number can be expressed in terms of the relevant forces, i.e. $Ar =$ (inertial force)(gravitational force)/(viscous force)$^2$. During the ring growth, the ring accelerates the surrounding liquid, so that the orders of the dynamic pressure and the area of the associated liquid motion are estimated as $\rho_0 \dot{R}^2$ and $\pi R^2$, respectively. The order of magnitude of the inertial force, $F_i$, is therefore expressed as

$$F_i \sim \rho_0 \dot{R}^2 \cdot \pi R^2 \tag{13}$$

Equation (9) is the relation between the gravitational and viscous forces and does not include the inertial force as discussed above. At large $Ar$, the inertial force may play a role in the rate of ring growth rather than $F_g$. We therefore assume that

$$F_\mu \sim c' F_i \tag{14}$$

where $c'$ is a constant. Substituting Eqs. (11) and (13) into Eq. (14) yields

$$\frac{\alpha}{\nu} = c \tag{15}$$

where $c = 4/c'$. Equations (9) and (15) intersect with each other at a certain Archimedes number, $Ar_c$, i.e. equating these equations yields

$$Ar_c = \frac{c - c_2}{c_1} \tag{16}$$

Equations (9) and (15) are combined as

$$\frac{\alpha}{\nu} = \begin{cases} c_1 Ar + c_2 & \text{for } Ar < Ar_c \\ c & \text{for } Ar \geq Ar_c \end{cases} \tag{17}$$

or this can be simply rewritten as

$$\frac{\alpha}{\nu} = \min\left(c_1 Ar + c_2, c\right) \tag{18}$$

Since Eq. (9) can give reasonable predictions up to $Ar = 100$ and the predictions deviate from the data of larger $Ar$, let us take $Ar_c = 100$, so that $c = 4.14$.

Predictions with Eq. (18) are shown by the closed circles in Fig. 6. The closed circles collapse onto a single curve at $Ar \approx 200$ and the scatter of the predictions is smaller than that with Eq. (9). Interestingly, the simple modification in the $\alpha$ correlation reproduces the slight reduction in $\overline{m}$ between the present data of $Ar = 290$ and 930, and the predictions fairly agree with them. Substituting Eq. (18) into Eq. (6) yields

$$\Gamma = \frac{4}{3} \frac{\mu_0 \Delta\rho g r^3}{\min\left(c_1 \Delta\rho g r^3 + c_2 \mu_0^2, c\mu_0^2\right)} \tag{19}$$

Figure 7 shows $\Gamma$ evaluated using Eq. (19), where $\Delta\rho$ is the parameter, and the other conditions are set for a drop of $r = 1.68$ mm falling into water. The $\Gamma$ decreases with increasing $\Delta\rho$ at low $\Delta\rho$, for which $\alpha/\nu$ depends on $Ar$. In contrast, $\Gamma$ increases with increasing $\Delta\rho$ for the constant $\alpha/\nu$. In the latter regime, the predicted $\overline{m}$ is almost constant even with the increase in $Ar$. The relation between $\Gamma$ and $\overline{m}$ is consistent with numerical results (Shimokawa et al., 2016) that the strong circulation makes the ring stable. By estimating the drop velocity, $U$, at the moment of the impact on the free surface as 0.3 m/s, the order of the produced circulation can be estimated as $\Gamma \sim Ur = 5 \times 10^{-4}$ m$^2$/s, which confirms that the order of $\Gamma$ evaluated with the $\alpha/\nu$ correlation is reasonable.

Thus, the good agreements between the predictions and the data support the validity of the modeling based on the Rayleigh-Taylor instability for the large $Ar$ systems.

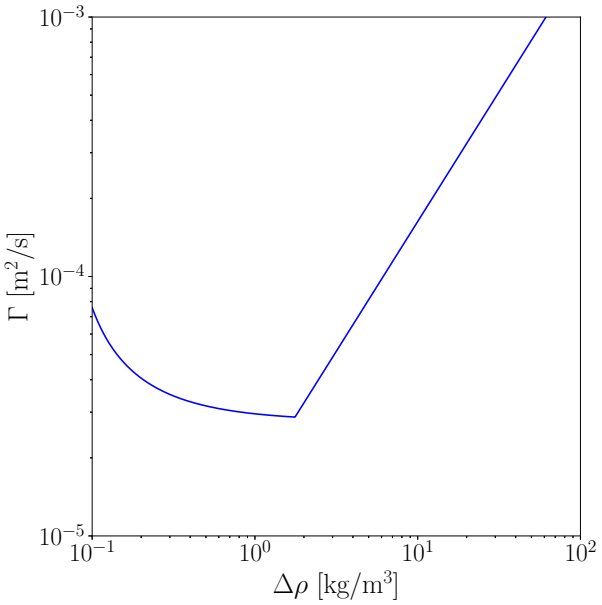


Figure 7: Circulation, $\Gamma$, evaluated with $\alpha/\nu$ correlation.

### *3.2. Fragmentation of two drops under their interaction*

#### *3.2.1. Comparison of relative frequency densities of leading and trailing drops*

The radii, $r_{2;1}$ and $r_{2;2}$, of the leading and trailing drops were 1.69 mm and the uncertainties in the mean radii at 95% confidence were 0.02 mm, where the subscripts $2;1$ and $2;2$ denote the leading and trailing drops, respectively. Therefore, $Ar = 290$ as well as in the single-drop experiment. Figure 8 shows $f(m)$ of leading and trailing drops. The $f_{2;1}(m)$ has its peak at $m = 4$ and the nearly-symmetric bell-bottom shape is similar to $f_1(m)$. In comparison with $f_{2;1}(m)$, $f_{2;2}(m)$ shifts toward the small $m$ side and the peak appears at $m = 3$. The distribution of $f_{2;2}$ is no longer Gaussian distribution. This point will be discussed later. The $\overline{m}_{2;1}$ and $\overline{m}_{2;2}$ are 4.20 and 3.46, respectively, and both of them are smaller than $\overline{m}_1$, which clearly shows that the drop-drop interaction mitigates the fragmentation, especially for the trailing drop. In addition, a noticeable difference from $f_1(m)$ is that $f_{2;2;}(1)$ takes a large value.

The falling motion of a leading drop induced a downward flow in the bulk liquid. Consequently, a part of or the whole of the trailing drop was drawn toward the center of the leading vortex ring. The probability of cases without the suction of trailing drop was only

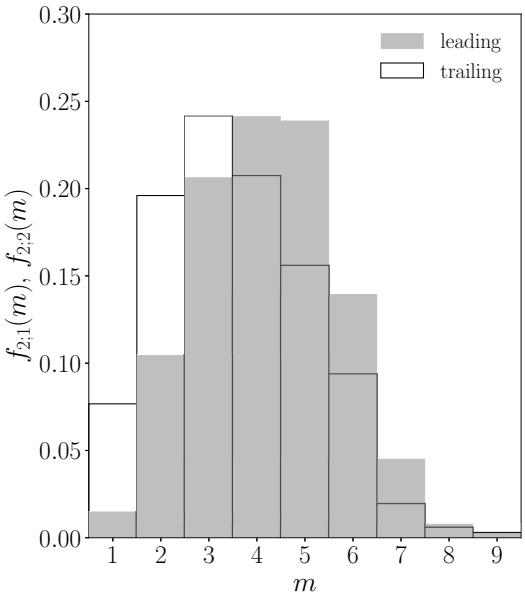


Figure 8: Relative frequency densities, $f_{2;1}(m)$ and $f_{2;2}(m)$, of fragmentation of leading and trailing drops. $\overline{m}_1$ and $\overline{m}_2$ are 4.20 and 3.46, respectively, for the sample sizes of 403 and 352.

1% in over 500 times observations, and therefore, those cases will be excluded in the following discussion. In the following, the drop-drop interactions are classified into three typical types and the effects of the interaction on the fragmentation are discussed for each type.

*3.2.2. Classification of interaction types*

The interaction types were classified into either type A, B or C. These types appeared at the probability of 26, 54 and 19%, respectively, in 457 samples. The motion of drops in these types are as follows:

A: An example of the drops in type A is shown in Fig. 9. The trailing drop rapidly approaches the leading drop (a). At this moment, the leading vortex ring already fragments, while the radius of the trailing vortex ring is not large enough for fragmentation. The trailing ring passes through the leading ring ((b)-(d)). An enlargement of the radius of the leading ring like a leapfrogging motion of two coaxial rings (Lim, 1997; Sommerfeld, 1964; Kojima et al., 1984) does not take place since the opening of the leading ring is large enough for the passage of the trailing ring. The onset of

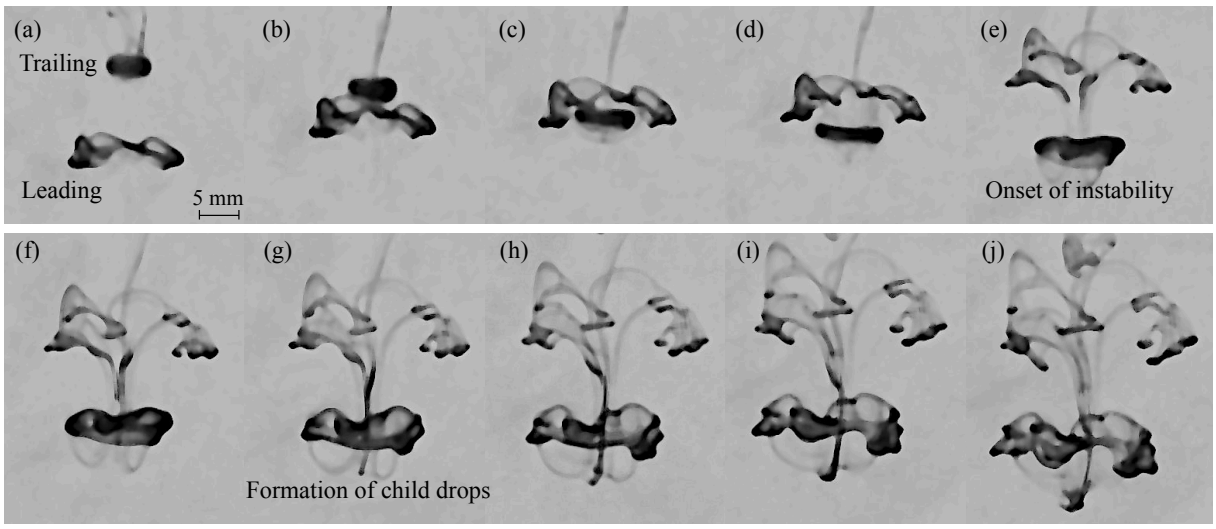


Figure 9: Fragmentation of two drops under drop-drop interaction classified in type A. (a) $t = t_1$; (b) $t_1 + 0.33$ s; (c) $t_1 + 0.67$ s; (d) $t_1 + 1$ s; (e) $t_1 + 2.33$ s; (f) $t_1 + 3$ s; (g) $t_1 + 3.67$ s; (h) $t_1 + 4.33$ s; (i) $t_1 + 5$ s; (j) $t_1 + 5.67$ s, where $t_1 = 3.5$ s.

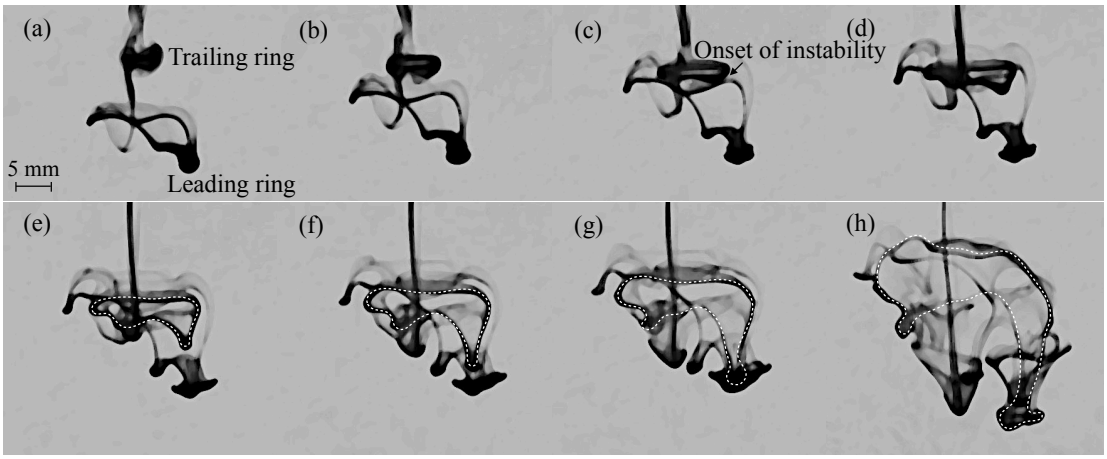


Figure 10: Fragmentation of two drops under drop-drop interaction classified in type B. (a) $t = t_1$; (b) $t_1 + 0.67$ s; (c) $t_1 + 1.33$ s; (d) $t_1 + 2$ s; (e) $t_1 + 2.67$ s; (f) $t_1 + 3.33$ s; (g) $t_1 + 4$ s; (h) $t_1 + 6.67$ s, where $t_1 = 3.8$ s. The dashed lines represent the outline of the trailing ring.

325 instability of the trailing ring then occurs in (e) followed by the formation of child drops ((g)-(j)).

B: Figure 10 shows a typical example of type B. In Fig. 10(a), the leading vortex ring is breaking up into some child drops. The trailing ring is present above the leading

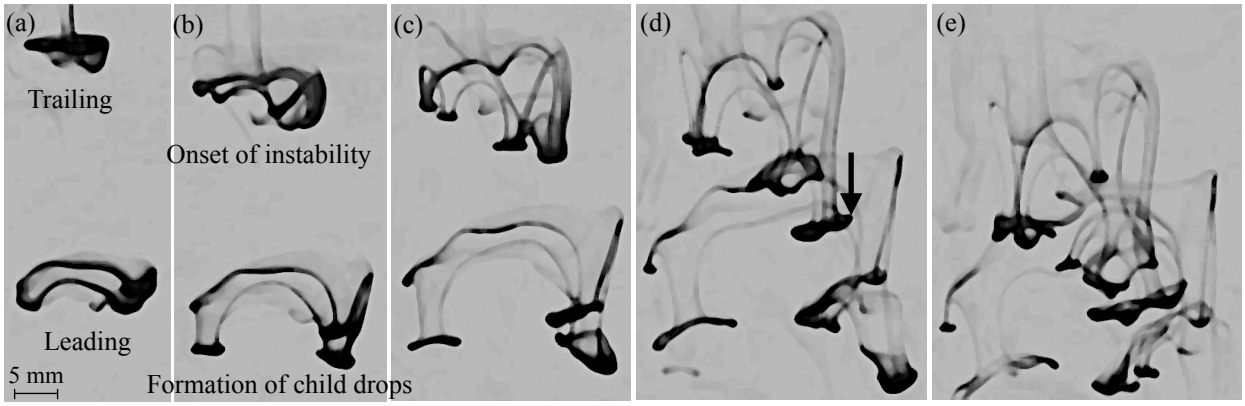


Figure 11: Fragmentation of two drops under drop-drop interaction classified in type C. (a) $t = t_1$; (b) $t_1 + 2$ s; (c) $t_1 + 4.7$ s; (d) $t_1 + 6.7$ s; (e) $t_1 + 8.7$ s, where $t_1 = 4.4$ s.

ring. The trailing ring expands laterally (b) and the onset of instability takes place (c). During its fragmentation event, the trailing ring is falling down through the center region of the leading ring ((d)-(h); the trailing drop is outlined by the dashed lines from (e)).

C: In type C, fragmentation of both leading and trailing vortex rings takes place before direct interaction. In Fig. 11(a), the first fragmentation of the leading ring begins. The onset of instability of the trailing ring is observed in (b), in which some child drops are formed from the leading ring. The fragmentation of the trailing ring proceeds in (c). The leading ring expands wider than the trailing ring. The child drops produced from the trailing ring catch up the leading ring (d) and go through the center region of the leading ring (e).

### *3.2.3. Fragmentation in each interaction type*

Figure 12(a) shows the relative frequency densities, $f(h_F)$, of $h_F$ of leading and trailing drops in type A, where $f_1(h_F)$ of single drops is also drawn for comparison and the width, $\Delta_h$, of the bin for the histogram is 10 mm. Most data of leading drops are less than 30 mm as in the single-drop case, i.e. $\sum_{h_F<30\ \mathrm{mm}} f_{2;1}(h_F)\Delta_h = 0.94$ and $\sum_{h_F<30\ \mathrm{mm}} f_1(h_F)\Delta_h = 0.85$. However, the distribution of $f_{2;1}(h_F)$ is much sharper than that of $f_1(h_F)$. The $f_{2;2}(h_F)$ is relatively large in the large $h_F$ range, i.e. $\sum_{h_F>30\ \mathrm{mm}} f_{2;2}(h_F)\Delta_h = 0.85$, since

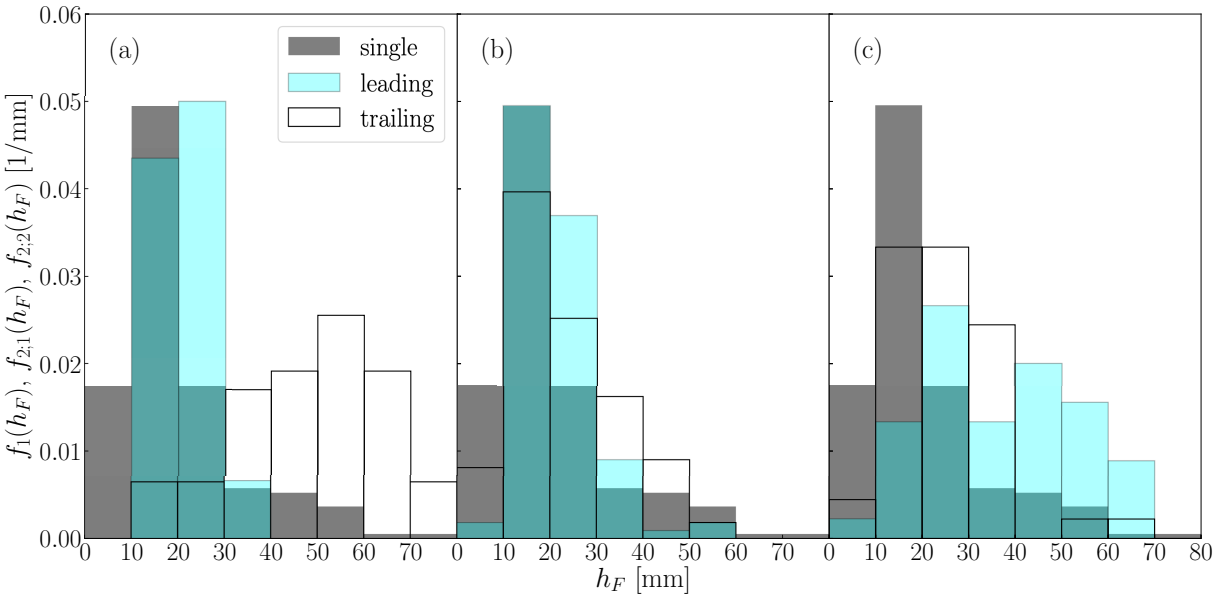


Figure 12: Relative frequency densities, $f_{2;1}(h_F)$ and $f_{2;2}(h_F)$, of fragmentation position. $f_1(h_F)$ is also plotted for comparison.

the trailing drops fragmented after passing through the leading drops. In average, the onset of fragmentation of trailing drops took place at 47 mm, whereas the mean $h_F$ of the leading drop was 21 mm. Figure 12(b) shows $f_{2;1}(h_F)$ of type B, which is similar to that of type A. Though the former is slightly broader, the mean $h_F$ of leading drops of types A and B are close. The mean $h_F$ of trailing drops (24 mm) is slightly larger than that of leading drops but not so different. In type C, the fragmentation of leading drops tended to take place at deeper positions as shown in Fig. 12(c) and the mean $h_F$ is 37 mm. On the other hand, the influence of drop-drop interaction on $h_F$ of the trailing drops could be weaker compared with types A and B, so that most of the trailing drops fragmented for $h_F < 40$ mm and the mean $h_F$ ($= 25$ mm) is similar to the mean values of leading drops in types A and B.

As discussed above, most single drops fragmented for $h_F < 30$ mm, and the ratio of the drops fragmented for $h_F > 30$ mm to the total number of samples was 16%. When leading drops in the two-drop experiment fragmented at deep positions like the single drops of 16%, the probability of the occurrence of type C could be high. Since the probability of $h_F > 30$ mm for leading drops is much less than that of $h_F < 30$ mm, type C took place at

the lowest probability, i.e. 19%. In type A, the trailing drop quickly approached the leading drop. There is a possibility that the motion of the trailing drop of type A is similar to that of the leading drop of type C. This speculation partly describes the probability of this interaction type, 26%. Another possibility is that an influence of the disturbance of the free surface due to the impact of the leading drop. The leading drop caused some surface waves on the free surface. If the trailing drop impacted on the free surface at the moment that the surface was in a downward motion of oscillation, the trailing drop could come smoothly into the pool. The surface motion in the opposite direction may somewhat contribute to the occurrence of type C. Type B was the most probable interaction type (54%). As can be seen in $f_{2;1}(h_F)$ and $f_{2;2}(h_F)$ of this type, the deviations from $f_1(h_F)$ are the smallest among the three types. This implies that the falling motions of both the leading and trailing drops were similar to those of single drops and consequently the two drops fragmented nearby. In addition, the influence of the disturbances on the free surface induced by the leading drop is considered to be not significant at least in this interaction type.

Let us discuss the characteristics of $f_{2;2}(m)$ in each interaction type. Figure 13 shows $f_{2;2}(m)$ (the white bars) in comparison with $f_1(m)$ (the gray bars). In type A (a), $f_{2;2}(m)$ of $m \geq 4$ are smaller than $f_1(m)$, while $f_{2;2}(m)$ of $m \leq 3$ are larger, i.e., the interaction type A suppresses the number of child drops. This implies that the vortical liquid flow induced by the leading ring around it somewhat suppresses the lateral growth of the trailing ring while passing through the center region of the leading ring. The decrease in the growth rate, $\alpha$, of the ring results in a reduction of $m$ as seen in the numerical predictions for single drops. Even with the $m$ reduction, the difference in the shape between $f_{2;2}(m)$ and $f_1(m)$ is not remarkable. Therefore, the reduction effect on $f_{2;2}(m)$ in type A may be expressed by a simple shift of the distribution, that is,

$$f_{2;2}(m) \leftarrow f_1(m+1) \quad \text{for} \quad m \geq 1 \tag{20}$$

where the arrow represents substitution. The $f_{2;2}$ obtained with this equation is shown by the thin bars in the figure.

Mitigation of the fragmentation of trailing drops is more obvious in type B (b). The

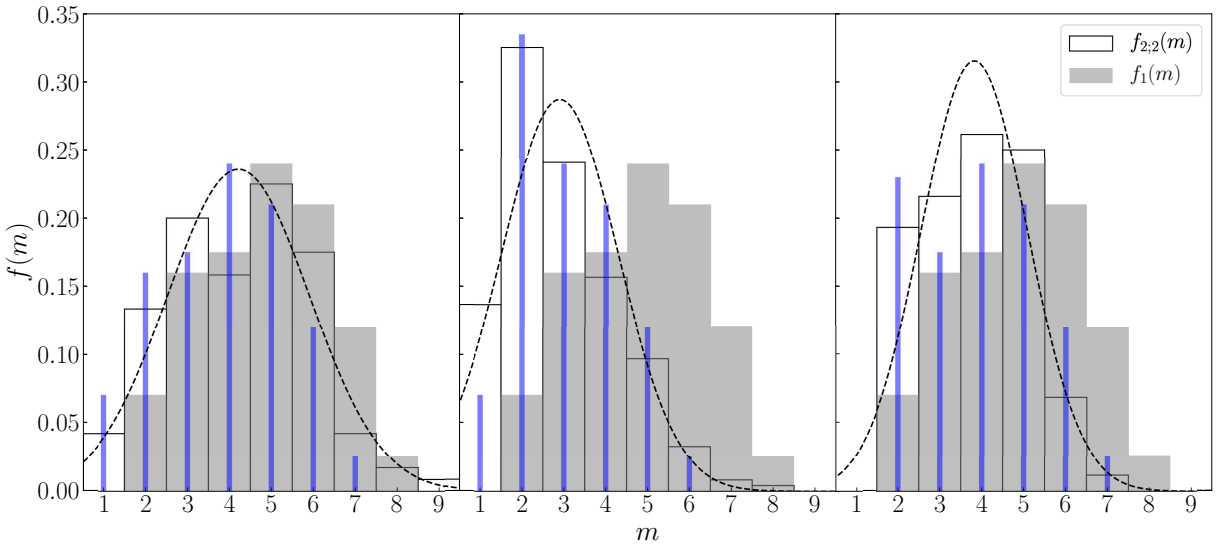


Figure 13: Relative frequency density, $f_{2;2}(m)$, of trailing drop. White: trailing drop, gray: single drop. Dashed lines: Gaussian distribution for mean and standard deviation of $f_{2;2}(m)$.

$f_{2;2}(m)$ for $m \geq 5$ are remarkably reduced by the influence of the leading drop and less than 0.10. On the other hand, $f_{2;2}(2)$ is much larger than $f_1(2)$. The fragmentation requires an enough volume, in other words an enough gravitational force. When a part of the trailing ring is pulled by the downward flow produced by the leading ring, the remaining part is stretched and consequently the thinned part of the ring fragments at a lower probability. Another key feature in $f_{2;2}(m)$ is the large value of $f_{2;2}(1)$. An example of drops of $m_{2;2} = 1$ is shown in Fig. 14. The leading ring fragments and child drops are formed in Fig. 14(a). The trailing ring above the leading ring is largely deformed. A large amount of the trailing ring is drawn by the downward flow produced by the falling motion of the leading ring and behaves like a child drop of large size ((b)-(j); the trailing ring is outlined by the dashed line). The remaining part of the ring is largely stretched. It becomes thinner and thinner and no fragmentation takes place there. The main reason of the breakup of $m_{2;2} = 1$ is therefore the stretch by the downward flow. The mode of $m_{2;2} = 1$, from this point of view, should be regarded as an advection-induced breakup. If a large amount of the ring volume is drawn by the downward liquid flow, disturbances in the remaining part of the trailing

ring would lose a chance to grow. In order to express the large $m$ reduction, a shift with the wider stride is applied for $f_1(m \geq 3)$: $f_{2;2}(m) \leftarrow f_1(m+2)$. Since $f_{2;2}(1) \neq 0$ in type B, let us set $f_{2;2}(m) \leftarrow f_1(m+1)$ for $m = 1$. The most probable mode is $m = 2$ in type B, so that $f_1(3)$ and $f_1(4)$ are stacked on $f_{2;2}(2)$. Thus,

$$\begin{aligned} f_{2;2}(m) &\leftarrow f_1(m+2) && \text{for} \quad m \geq 3 \\ f_{2;2}(m) &\leftarrow f_1(m+1) + f_1(m+2) && \text{for} \quad m = 2 \\ f_{2;2}(m) &\leftarrow f_1(m+1) && \text{for} \quad m = 1 \end{aligned} \tag{21}$$

The $f_{2;2}$ given by this equation agrees fairly well with the data as shown by the thin bars in the figure.

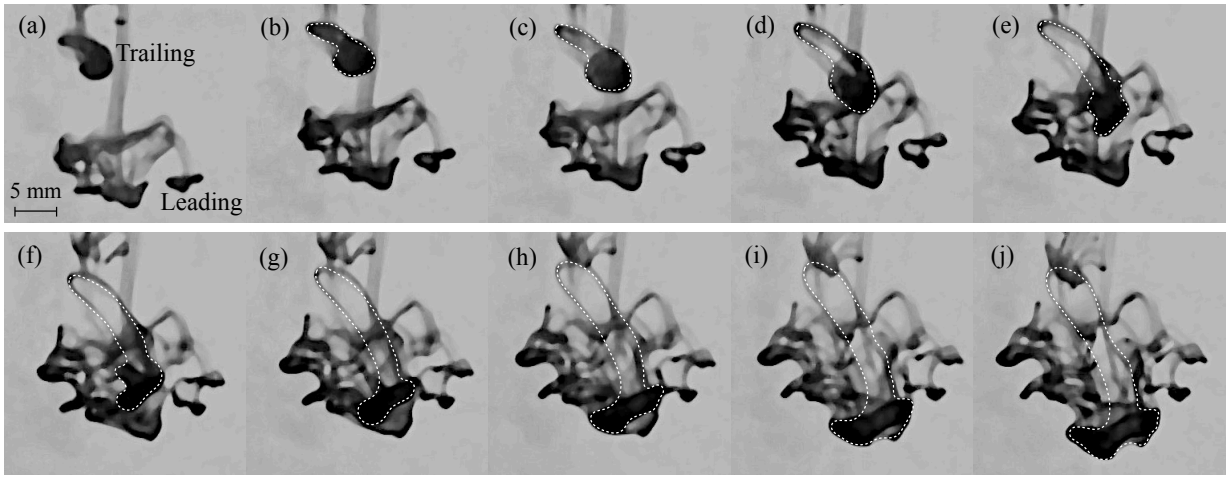


Figure 14: Motion of drop of $m_{2;2} = 1$. (a) $t = t_1$; (b) $t_1 + 0.33$ s; (c) $t_1 + 0.67$ s; (d) $t_1 + 1$ s; (e) $t_1 + 1.33$ s; (f) $t_1 + 1.67$ s; (g) $t_1 + 2$ s; (h) $t_1 + 2.33$ s; (i) $t_1 + 2.67$ s; (j) $t_1 + 3$ s, where $t_1 = 3.5$ s. The dashed lines represent the outline of the trailing ring.

In type C (c), the shape of the distribution of $f_{2;2}(m)$ is similar to $f_1(m)$, whereas the distribution is shifted to the small $m$ side and $f_{2;2}(2)$ is much larger than $f_1(2)$. In spite of that the trailing ring fragments apart from the leading ring, the leading ring can affect $m_{2;2}$ via the flow in the bulk liquid induced by the leading ring, i.e., the downward flow produced by the leading ring attenuates the lateral growth of the trailing ring, in other words the growth rate $\alpha$, the reduction of which possibly results in the decrease in $m$. The effect of the leading drop on the behavior of the trailing drop can also be seen in $h_F$, i.e. the trailing

drops fragment at positions somewhat deeper than the single drops. Being similar to type A, a simple shift of $f_1(m)$ gives a reasonable expression of $f_{2;2}(m)$, i.e.

$$\begin{aligned} f_{2;2}(m) &\leftarrow f_1(m+1) && \text{for} \quad m \geq 3 \\ f_{2;2}(m) &\leftarrow f_1(m) + f_1(m+1) && \text{for} \quad m = 2 \end{aligned} \tag{22}$$

where $f_1(3)$ is stacked on $f_{2;2}(2)$ since $f_{2;2}(1)$ does not appear in type C.

It would be important to mention that, in all the interaction types, no breakup enhancement occurred. The $\overline{m}_{2;2}$ are 4.2, 2.9 and 3.8 in types A, B and C, respectively. The simple modifications of $f_1(m)$ reproduce the effects of the drop-drop interaction on $f_{2;2}(m)$ fairly well. As can be seen in the modification, the shapes of $f_{2;2}(m)$ in types B and C are no longer normal distribution (the dashed lines), i.e., the $\chi^2$ test rejects the hypothesis of similarity between them at 5% significance level.

The time intervals, $\Delta t$, between two drops were 3.00 s in all the experimental runs. Longer $\Delta t$ would decrease possibilities of interactions between two drops, so that the probability of type C would increase. If $\Delta t$ was too short, a violent collision between the leading and trailing drops could occur before the onset of fragmentation. The position of the leading drop at the moment of the impact of the trailing drop was not constant, but exhibited some scatter. Therefore, not only $\Delta t$, but also the initial distance between the two drops should be taken as a parameter for further analysis. The drop impact velocity was also unchanged in the present experiment due to the fixed needle position. Changing the needle position possibly affects the initial distance between the two drops in water. The effects of the relevant parameters on the fragmentation pattern and $m$ remain as a future work.

## 4. Conclusion

In this study, experiments on liquid drops falling through a miscible liquid were carried out to investigate the characteristics of fragmentation of single drops at large Archimedes numbers, $Ar$ (= 290, 480 and 930), and the effects of drop-drop interaction on the number, $m$, of child drops produced from the parent vortex ring. As a result we obtained the following conclusions:

- The $m$ of single drops exhibits a random nature and distributes in a wide range. Its probability can be approximated by the normal distribution.

- An empirical correlation of the mean $m$ was obtained and it can give reasonable evaluations for experimental conditions of the present and Shimokawa and Sakaguchi (2019).

- A numerical method developed for $Ar \leq 80$ (Shimokawa and Sakaguchi, 2019) is applicable to the present single drop case by modifying the correlation of the growth rate of a ring radius, which supports the validity of the modeling based on the Rayleigh-Taylor instability.

- The types of interactions between two falling drops are classified into three types: (A) the trailing vortex ring passes through the leading vortex ring and then fragments, (B) the fragmentation of the trailing ring begins above the leading ring, while the downward liquid flow produced by the leading ring draws a part of the trailing ring during its fragmentation, and (C) the fragmentation of the trailing ring almost completes before passing through the leading ring.

- In type A, $m$ of the trailing ring is decreased by the presence of the leading ring, which shifts the probability of $m$ toward the small $m$ side. In type B, the trailing ring is largely stretched by the downward liquid flow, which results in a significant reduction in $m$ of the trailing ring. In type C, in spite of the distance of several times longer than the drop radius between two drops during their fragmentation, the presence of the leading drop can affect the fragmentation of the trailing drop so as to reduce $m$.

**Acknowledgement**

The authors would like to express their sincere thanks to Mr. Naoyuki Yoshida (Kobe University) for his assistance in the experiments and to the JST Global Science Campus ROOT Program for supporting this study.

## Appendix A. Single drop experiment for $Ar < 100$

Though the aim of the present study is to understand the behaviors of drops at the Archimedes numbers larger than those investigated in the literature ($Ar < 80$) (Shimokawa and Sakaguchi 2017, 2019), we carried out additional single-drop experiments for $Ar < 100$ to confirm the consistency of the $\overline{m}$ data with those in the literature. The experiments were carried out using water with the red-food color (0% aqueous-NaCl solution) and 0.2% aqueous-NaCl solution at 16°C. The density difference between the bulk and drops in the former condition was due to the addition of the coloring agent. The density differences, $\Delta\rho$, considering the effect of the coloring agent were 0.3 and 2.2 kg/m$^3$ for the former and the latter, respectively. A syringe needle (Terumo, NN-2738R) was used for the former solution. This needle is finer than that used in the experiments with the 0.6% and 2.2% NaCl solutions. The mean drop radius was $1.69 \pm 0.07$ mm and $Ar$ was 13. For the 0.2% NaCl solution, both needles were used and the resultant drop radii were $1.39 \pm 0.04$ mm and $1.77 \pm 0.04$ mm and, for these $r$, $Ar = 47$ and 97, respectively.

Figure A.1 shows the relative frequency densities, $f_1(m)$. The $f_1(m)$ take larger values at small $m$ compared with those for $Ar > 100$, whereas $m = 1$ does not take place whatever $Ar$ is. The shapes of the probability distributions are thus distorted and deviate from the normal distributions. The mean, $\overline{m}$, are 2.78, 4.27 and 3.88 at $Ar = 13$, 47 and 97, respectively, and are plotted in Fig. 5. Comparing the present data with those in the literature shows a reasonable agreement between them. The $\overline{m}$ at $Ar = 97$ is slightly smaller than that at $Ar = 47$. The fluids were the same in these conditions and only difference was in $r$. Because of the larger $r$, the circulation, $\Gamma$, could be larger in the latter. Shimokawa et al. (2016) pointed out that the increase in $\Gamma$ suppresses the growth of instability. This give a possible reason of the difference in $\overline{m}$. The scatter of the data and the standard deviation of $m$ in Fig. 5 are relatively large for $40 < Ar < 100$. Interestingly, the numerical predictions shown in Fig. 6 give a similar trend although more data and analysis are required to understand the dynamics of fragmenting vortex rings in this transition regime.

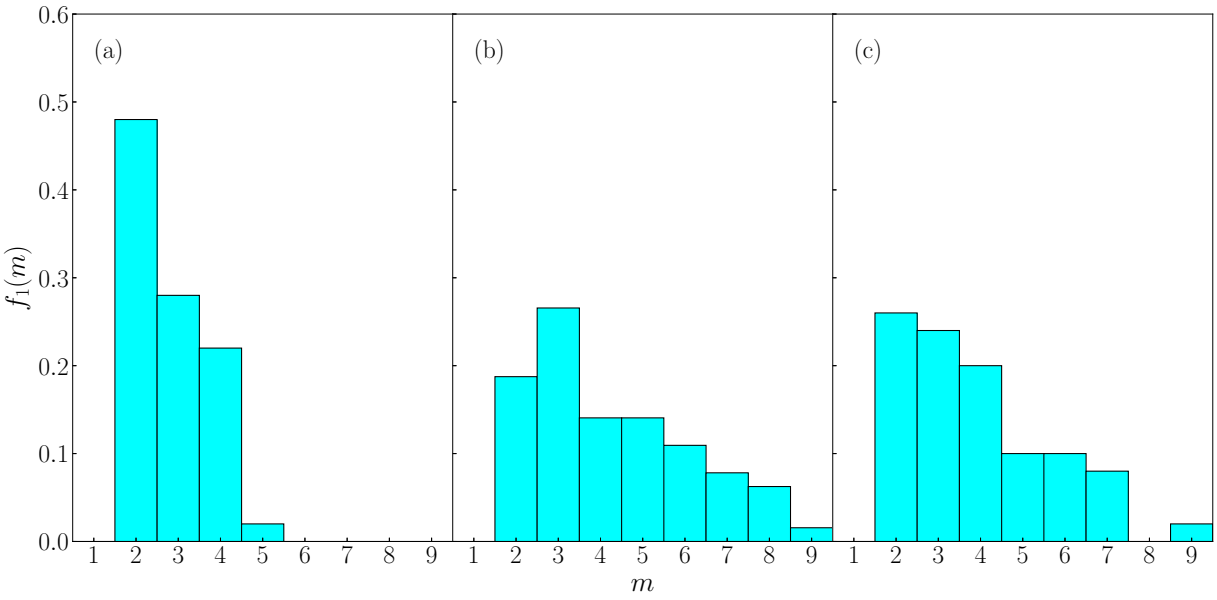


Figure A.1: Relative frequency densities, $f_1(m)$, of single drops at $Ar < 100$. (a) $Ar = 13$; (b) $Ar = 47$; (c) $Ar = 97$. $\overline{m} = 2.78$, 4.27 and 3.88 and the number of samples are 50, 64 and 50 in (a), (b) and (c), respectively.

## Appendix B. Model for evaluating $n(k)$

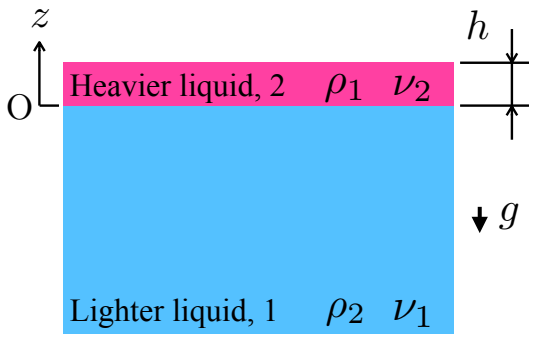


Figure B.2: Two-layer model

Shimokawa et al. (2016) used the two-layer model shown in Fig. B.2 to evaluate the
495 rate, $n(k)$, of growth due to Rayleigh-Taylor instability (Harrison, 1908; Chandrasekhar, 1981). The heavier liquid, 2, of the finite thickness, $h$, is superposed on the lighter liquid, 1, of infinite depth. The velocity component, $w$, in the $z$ direction and its derivative is

continuous at the interface between the liquids, i.e.

$$z = 0: \qquad w_1 = w_2, \quad dw_1/dz = dw_2/dz \tag{B.1}$$

The liquid 1 is stagnant far from the interface:

$$z \to -\infty: \qquad w_1 \to 0 \tag{B.2}$$

The top boundary of the liquid 2 at $z = h$ is assumed to be no-slip:

$$z = h: \qquad w_2 = \frac{dw_2}{dz} = 0 \tag{B.3}$$

For the normal mode in the form of $e^{ik_x x + ik_y y + nt}$, we also have the following boundary conditions in the absence of surface tension:

$$\begin{aligned} z = 0: \qquad & \left[\rho_2 - \frac{\mu_2}{n}\left(\frac{d^2}{dz^2} - k^2\right)\right]\frac{dw_2}{dz} - \left[\rho_1 - \frac{\mu_1}{n}\left(\frac{d^2}{dz^2} - k^2\right)\right]\frac{dw_1}{dz} \\ & = -\frac{gk^2}{n^2}(\rho_2 - \rho_1)w_0 - \frac{2k^2}{n}(\mu_2 - \mu_1)\left.\frac{dw}{dz}\right|_0 \end{aligned} \tag{B.4}$$

and

$$z = 0: \qquad \mu_2\left(\frac{d^2}{dz^2} + k^2\right)w_2 = \mu_1\left(\frac{d^2}{dz^2} + k^2\right)w_1 \tag{B.5}$$

where $x$ and $y$ are the Cartesian coordinates on the horizontal plane, $k_x$ and $k_y$ are the wave numbers in those directions, $k^2 = k_x^2 + k_y^2$, $t$ is the time, and the subscript 0 denotes the interface. The velocity components in the liquids have the following forms:

$$w_1 = A_1 e^{kz} + B_1 e^{q_1 z} \tag{B.6}$$

$$w_2 = A_2 e^{-kz} + B_2 e^{-q_2 z} + C_2 e^{kz} + D_2 e^{q_2 z} \tag{B.7}$$

Substituting these expressions of $w_1$ and $w_2$ into the above six boundary conditions and applying the condition that the constants are non-zero yield the characteristic equation for

$n(k)$:

$$\begin{vmatrix} 1 & 1 & -1 & -1 & -1 & -1 \\ k & q_1 & k & q_2 & -k & -q_2 \\ 0 & 0 & e^{-kh} & e^{-q_2 h} & e^{kh} & e^{q_2 h} \\ 0 & 0 & -ke^{-kh} & -q_2 e^{-q_2 h} & ke^{kh} & q_2 e^{q_2 h} \\ M_{51} & M_{52} & M_{53} & M_{54} & M_{55} & M_{56} \\ M_{61} & M_{62} & M_{63} & M_{64} & M_{65} & M_{66} \end{vmatrix} = 0 \tag{B.8}$$

where

$$M_{51} = 2k^2\mu_1 \tag{B.9}$$

$$M_{52} = (q_1^2 + k^2)\mu_1 \tag{B.10}$$

$$M_{53} = M_{55} = -2k^2\mu_2 \tag{B.11}$$

$$M_{54} = M_{56} = -(q_2^2 + k^2)\mu_2 \tag{B.12}$$

$$M_{61} = \frac{R}{2} - C - \alpha_1 \tag{B.13}$$

$$M_{62} = \frac{R}{2} - \frac{q_1}{k}C \tag{B.14}$$

$$M_{63} = \frac{R}{2} + C - \alpha_2 \tag{B.15}$$

$$M_{64} = \frac{R}{2} + \frac{q_2}{k}C \tag{B.16}$$

$$M_{65} = \frac{R}{2} - C + \alpha_2 \tag{B.17}$$

$$M_{66} = \frac{R}{2} - \frac{q_2}{k}C \tag{B.18}$$

$$q_i = k^2 + \frac{n}{\nu_i} \quad (i = 1 \text{ or } 2) \tag{B.19}$$

$$\alpha_i = \frac{\rho_i}{\rho_1 + \rho_2} \quad (i = 1 \text{ or } 2) \tag{B.20}$$

$$R = -\frac{gk}{n^2}(\alpha_1 - \alpha_2) \tag{B.21}$$

$$C = \frac{k^2}{n}(\alpha_1 \nu_1 - \alpha_2 \nu_2) \tag{B.22}$$

We iteratively solved this equation for $n(k)$ and evaluated $A_m(t)$ (Eq. (8)). The $h$ corresponding to the thickness of a vortex ring was given as $h(t) = [2V/(\pi^2 R(t))]^{1/2}$.

In the two-layer model, $w_2$ and $dw_2/dz$ are set to zero at $z = h$. However, in the experiments, the lighter liquid is on the vortex ring, and therefore, in the model the third liquid layer of infinite thickness can be placed on the heavier liquid, 2, and the boundary conditions at $z = h$ can be those for fluid-fluid interfaces, i.e. the three-layer model (Parhi and Nath, 1991). Figure B.3 shows a comparison between $n(k)$ of the two- and three-layer models. Although the trends are the same, $n$ of the former is lower than that of the latter especially for small thickness $h$, that is, the boundary condition of $w_2 = 0$ in the two-layer model mitigates the growth of perturbations. We also carried out the numerical simulations in Sec. 3.1.2 with the three-layer model. The results, however, worse than those with the two-layer model. This might be because the model parameters and correlations were optimized/developed for the two-layer model (Shimokawa and Sakaguchi, 2019) and we should reconsider the parameters and correlations based on experimental data, if we employed the three-layer model.

The equation for $n(k)$ in the three-layer model is given below for reference.

$$\begin{vmatrix} 1 & 1 & -1 & -1 & -1 & -1 & 0 & 0 \\ k & q_1 & k & q_2 & -k & -q_2 & 0 & 0 \\ 0 & 0 & e^{-kh} & e^{-q_2 h} & e^{kh} & e^{q_2 h} & -e^{-kh} & -e^{-q_3 h} \\ 0 & 0 & -ke^{-kh} & -q_2 e^{-q_2 h} & ke^{kh} & q_2 e^{q_2 h} & ke^{-kh} & q_3 e^{-q_3 h} \\ M_{51} & M_{52} & M_{53} & M_{54} & M_{55} & M_{56} & 0 & 0 \\ M_{61} & M_{62} & M_{63} & M_{64} & M_{65} & M_{66} & 0 & 0 \\ 0 & 0 & M_{73} & M_{74} & M_{75} & M_{76} & M_{77} & M_{78} \\ 0 & 0 & M_{83} & M_{84} & M_{85} & M_{86} & M_{87} & M_{88} \end{vmatrix} = 0 \tag{B.23}$$

where the subscripts 1, 2 and 3 stand for the lower, middle and upper liquids, respectively, and the components of the matrix are

$$M_{73} = 2k^2 \mu_2 e^{-kh} \tag{B.24}$$

$$M_{74} = (q_2^2 + k^2)\mu_2 e^{-q_2 h} \tag{B.25}$$

$$M_{75} = 2k^2 \mu_2 e^{kh} \tag{B.26}$$

$$M_{76} = (q_2^2 + k^2)\mu_2 e^{q_2 h} \tag{B.27}$$

$$M_{77} = -2k^2 \mu_3 e^{-kh} \tag{B.28}$$

$$M_{78} = -(q_3^2 + k^2)\mu_3 e^{-q_3 h} \tag{B.29}$$

$$M_{83} = \left( \frac{\widetilde{R}}{2} + \widetilde{C} + \widetilde{\alpha_2} \right) e^{-kh} \tag{B.30}$$

$$M_{84} = \left( \frac{\widetilde{R}}{2} + \frac{q_2}{k} \widetilde{C} \right) e^{-q_2 h} \tag{B.31}$$

$$M_{85} = \left( \frac{\widetilde{R}}{2} - \widetilde{C} - \widetilde{\alpha_2} \right) e^{kh} \tag{B.32}$$

$$M_{86} = \left( \frac{\widetilde{R}}{2} - \frac{q_2}{k}\widetilde{C} \right) e^{q_2 h} \tag{B.33}$$

$$M_{87} = \left( \frac{\widetilde{R}}{2} + \widetilde{C} - \alpha_3 \right) e^{-kh} \tag{B.34}$$

$$M_{88} = \left( \frac{\widetilde{R}}{2} + \frac{q_3}{k}\widetilde{C} \right) e^{-q_3 h} \tag{B.35}$$

$$\widetilde{\alpha_i} = \frac{\rho_i}{\rho_2 + \rho_3} \quad (i = 2 \text{ or } 3) \tag{B.36}$$

$$\widetilde{R} = -\frac{gk}{n^2}(\alpha_2 - \alpha_3) \tag{B.37}$$

$$\widetilde{C} = \frac{k^2}{n}(\alpha_2 \nu_2 - \alpha_3 \nu_3) \tag{B.38}$$

The definition of $q_i$ is the same as in the two-layer model, whereas the subscript $i$ takes either 1, 2 or 3.

## Appendix C. Effect of viscosity difference on growth rate of perturbations

The fragmentation is driven by the gravitational force, and therefore, the density difference is of primal importance. On the other hand, the viscosities of the fluids possibly mitigate instabilities leading to fragmentation of a vortex ring. We evaluated the effects of the viscosity difference between the two phases on the growth rate of the Rayleigh-Taylor instability as shown in Fig. C.4, where the fluid properties for water and 2.2% NaCl solution ($\rho = 1012$ kg/m$^3$, $\rho_0 = 997$ kg/m$^3$, $\mu = 0.93$ mPa·s and $\mu_0 = 0.89$ mPa·s) are used. It is clearly shown that the present magnitude of the viscosity difference does not substantially affect the growth rate of perturbations.

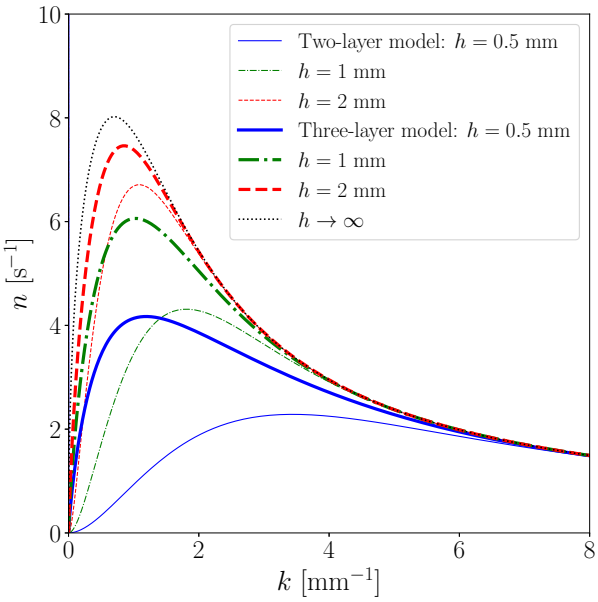


Figure B.3: Rates, $n(k)$, of growth evaluated using the two- and three-layer models.

## References


Arecchi, F. T., Buah-Bassuah, P. K., Francini, F., Perez-Garcia, C., Quercioli, F., 1989. An experimental investigation of the break-up of a liquid drop falling in a miscible fluid. Europhysics Letters 9(4), 333–338.

Arecchi, F. T., Buah-Bassuah, P. K., Francini, F., Residori, S., 1996. Fragmentation of a drop as it falls in a lighter miscible fluid. Physical Review E 54(1), 424–429.

Arecchi, F. T., Buah-Bassuah, P. K., Perez-Garcia, C., 1991. Fragment fromation in the break-up of a drop falling in a miscible liquid. Europhysics Letters 15(4), 429–434.

Chandrasekhar, S., 1981. Hydrodynamic and Hydromagnetic Stability. Dover.

Harrison, W., 1908. The influence of viscosity on the oscillations of superposed fluids. Proceedings of the London Mathematical Society s2-6(1), 396–405.

Kambe, T., Takao, T., 1971. Motion of distorted vortex rings. Journal of the Physical Society of Japan 31(2), 591–599.

Kojima, M., Hinch, E. J., Acrivos, A., 1984. The formation and expansion of a toroidal drop moving in a viscous fluid. The Physics of Fluids 27, 19–32.

Korteweg, D., 1901. Sur la forme que prennent les équations du mouvement des fluides si l'on tient compte des forces capillaires causées par des variations de densité considérables mais connues et sur la théorie de la capillarité dans l'hypothèse d'une variation continue de la densité. Archives Néerlandaises des Sciences Exactes et Naturelles Ser. II 6, 1–24.

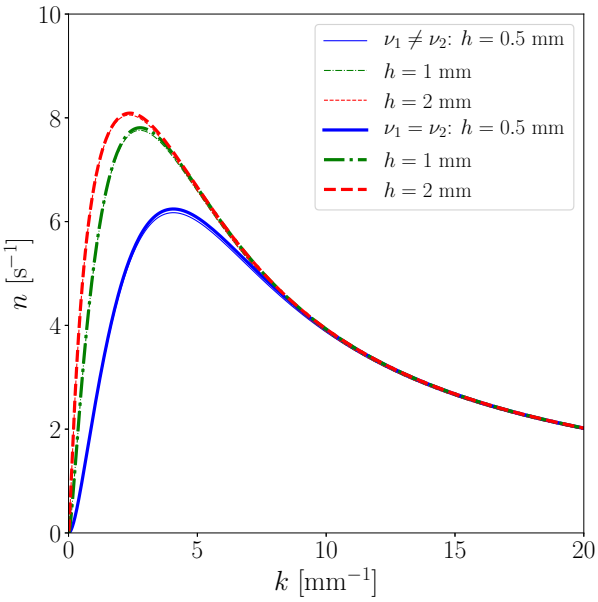


Figure C.4: Growth rate, $n_k$, of perturbations due to Rayleigh-Taylor instability. The solid lines are overlapped.


Kostin, I., Marion, M., Texier-Picard, R., Volpert, V. A., 2003. Modelling of miscible liquids with the Korteweg stress. ESAIM: Mathematical Modelling and Numerical Analysis 37(5), 741–753.

Lim, T., 1997. A note on the leapfrogging between two coaxial vortex rings at low Reynolds numbers. Physics of Fluids 9, 239–241.

Meleshko, V. V., 2010. Coaxial axisymmetric vortex rings: 150 years after helmholtz. Theoretical and Computational Fluid Dynamics 24, 403–431.

Meleshko, V. V., Gourjii, A. A., Krasnopolskaya, T. S., 2012. Vortex rings: history and state of the art. Journal of Mathematical Sciences 187(6), 772–808.

Oshima, Y., Kambe, T., Asaka, S., 1975. Interaction of two vortex rings moving along a common axis of symmetry. Journal of the Physical Society of Japan 38(4), 1159–1166.

Ozbek, H., Fair, J. A., Phillip, S. L., 1977. Viscosity of aqueous sodium chloride solutions from 0-150°c. Tech. rep., Lawrence Berkeley National Laboratory.

Parhi, S., Nath, G., 1991. A sufficient criterion for Rayleigh-Taylor instability of incompressible viscous three-layer flow. International Journal of Engineering Science 29(11), 1439–1450.

Residori, S., Buah-Bassuah, P. K., Arecchi, F. T., 2007. Fragmentation instabilities of a drop as it falls in a miscible fluid. The European Physics Journal Special Topics 146, 357–374.

Riquelme, R., Lira, I., Pérez-López, C., Rayas, J. A., Rodríguez-Vera, R., 2007. Interferometric measurement of a diffusion coefficient: comparison of two methods and uncertainty analysis. Journal of Physics D:

Applied Physics 40, 2769.

Rogers, P. S. Z., Pitzer, K. S., 1982. Volumetric properties of aqueous sodium chloride solutions. Journal of Physical and Chemical Reference Data 11 (1), 15–81.

Shimokawa, M., Mayumi, R., Nakamura, T., Takami, T., Sakaguchi, H., 2016. Breakup and deformation of a droplet falling in a miscible solution. Physical Review E 93, 062214.

Shimokawa, M., Sakaguchi, H., 2017. Deformation and breakup of a droplet falling into a viscous fluid (in japanese). Nihon Butsuri Gakkaishi 72(8), 570–575.

Shimokawa, M., Sakaguchi, H., 2019. Mode selection on breakup of a droplet falling into a miscible solution. Physical Review Fluids 4, 013603.

Sommerfeld, A., 1964. Mechanics of deformable bodies. Lectures on Theoretical Physics, Vol. II. Academic Press, New York.

Thomson, J. J., 1883. A treatise on the motion of vortex rings. An essay to which the Adams prize was adjudged in 1882, in the University of Cambridge. Macmillan, London.

Thomson, J. J., Newall, H. F., 1886. On the formation of vortex rings by drops falling into liquids. Proceedings of the Royal Society of London 39, 417–436.

Tomlinson, C., 1864a. On a new variety of the Cohesion-Figures of Liquids. The London, Edinburgh, and Dublin Philosophical Magazine and Journal of Science 27(184), 425–432.

Tomlinson, C., 1864b. On the cohesion-figures of liquids. The London, Edinburgh, and Dublin Philosophical Magazine and Journal of Science 28(190), 354–364.

Turner, J., 1957. Buoyant vortex rings. Proceedings of the Royal Society of London. Series A, Mathematical and Physical Sciences 239(1216), 61–75.